




Acoustically soft and mechanically robust hierarchical metamaterials in waterYang Wang,^{1,2} Honggang Zhao,^{1,2,*} Haibin Yang,^{1,2,†} Hongjia Zhang,^{1,2} Tao Li,^{1,2} Chao Wang^{1,2} ,^{1,2}
Jiawei Liu,^{1,2} Jie Zhong,^{1,2} Dianlong Yu,^{1,2} and Jihong Wen^{1,2,‡} ¹*College of Intelligence Science and Technology, National University of Defense Technology, Changsha 410073, People's Republic of China*²*Laboratory of Science and Technology on Integrated Logistics Support, National University of Defense Technology, Changsha 410073, People's Republic of China* (Received 19 February 2023; revised 18 September 2023; accepted 16 October 2023; published 7 November 2023)

Isolating noise in water relies on materials with low acoustic impedance. However, reducing the existing materials' acoustic impedance severely compromises their stiffness and strength, resulting in a long-standing challenge of sound isolation in deep-sea environments with high ambient pressure. To overcome the mutual exclusion of low acoustic impedance and high mechanical properties, we propose a design principle including two steps that regulate the lattice orientation and incorporate a hierarchical morphology in an anisotropic metamaterial. Regulating the lattice orientation leads to low effective acoustic impedance while counterintuitively improving the initial stiffness. By learning from nature, incorporating a hierarchical morphology enables the metamaterial with an unprecedented decoupling characteristic that the mechanical strength can be enhanced independently from the acoustic impedance. A hierarchical metamaterial is constructed as a proof-of-concept demonstration and displays high sound transmission loss over 16 dB in a low and broad frequency range from 400 to 1200 Hz. Of note, the hierarchical metamaterial could maintain stable acoustic performance even under a high ambient pressure of 2 MPa. This work not only opens an alternative avenue for realizing sound isolation in deep-sea environments but also offers a design principle for metamaterials combining antagonistic functional properties.

DOI: [10.1103/PhysRevApplied.20.054015](https://doi.org/10.1103/PhysRevApplied.20.054015)**I. INTRODUCTION**

Water encompasses over 70% of the Earth's surface, where rich underwater resources support the development of humanity [1]. With the ability of long-distance propagation, acoustic waves are the most potent information carrier for underwater sensing and communication [2,3]. However, noise interference is inevitable when receiving the desired acoustic signal [4]. To address this problem, underwater sound-isolation materials have attracted considerable interest [5–14].

Acoustic impedance mismatching is the fundamental principle for designing sound-isolation materials. For the common materials in nature, the effective acoustic impedance Z_e is a combination of the longitudinal phase wave speed c_l and density ρ_e , denoted by [15]

$$Z_e = \rho_e c_l. \quad (1)$$

When the propagating medium is air of extremely low acoustic impedance, materials with high densities commonly exhibit better sound-insulation performance than lightweight materials, according to the classical mass density law (MDL) [16]. In the last two decades, membrane-[17] and plate-type [18,19] acoustic metamaterials have been proposed to obtain superior air-borne sound-isolation performance than that derived from MDL.

Different from air, water belongs to high impedance media. The membrane- and plate-type metamaterials also with high impedance cannot efficiently isolate sound in the underwater environment. Even for a 50-mm-thick cumbersome steel immersed in water, over 85% of energy can pass through when the frequency of acoustic wave is below 500 Hz. In contrast to high-impedance materials, adopting low-impedance materials provides a more promising strategy. Under this guideline, the common underwater sound-isolation metamaterials consist of rubber with air inclusions [5,8,10,14]. The longitudinal phase speed and the acoustic impedance of these metamaterials can be significantly decreased with the filling ratio of air inclusions increased [20], resulting in efficient sound isolation in water. Nevertheless, in the underwater environment, the ambient pressure exists, and the amplitude

*zhhg9603@sina.com

†haibinyangsn@sina.com

‡wenjihong@vip.sina.com

increases by 0.1 MPa for every 10 m of water depth. With the filling ratio of air inclusions raised, the underwater sound-isolation metamaterials cannot control shape when the ambient pressure is increased, resulting in the collapse of air inclusions and decreases of the sound isolation in the low-frequency range [14]. Therefore, the mechanical robustness of underwater metamaterials should be highlighted.

Stiffness and strength are two fundamental properties to evaluate the mechanical robustness of materials. The stiffness, i.e., Young's modulus E_s , represents the material's initial capability to resist deformation at the linear elastic stage [21]. After the linear elastic stage, the metamaterials' instability may be triggered by either highly localized stress or long-wavelength modes, leading to maximum stress, i.e., strength σ_y , that indicates ultimate load-bearing capability [21]. High stiffness ensures small deformation of materials under the same ambient pressure, while high strength makes materials stable in deeper sea environments without yielding and failure. Therefore, an underwater sound-isolation material requires a combination of low acoustic impedance, high stiffness, and strength. Unfortunately, there are some conflicts among these three characteristics for conventional materials, which will be illustrated in the following.

One can see from Eq. (1) that low longitudinal phase speed is one choice for obtaining low acoustic impedance. But Young's modulus varies with the square of phase wave speed, leading to a conflict between low acoustic impedance and high stiffness. Reducing the density offers another choice for attaining low acoustic impedance. However, both stiffness and strength also drop with decreasing density through a power-law scaling [22–24] for many architectural materials, that is,

$$E/E_s = A\bar{\rho}^\alpha, \quad (2)$$

and

$$\sigma_y/\sigma_{ys} = B\bar{\rho}^\beta, \quad (3)$$

where $\bar{\rho}$ denotes the relative density, usually normalized by dividing the density of the constituent material. E_s and σ_{ys} are Young's modulus and strength of the constituent material, respectively, A and B are the proportionality constants, α and β are scaling exponents. Moreover, stiffness and strength are also not always positively correlated [21,25–27]. A metamaterial may possess high stiffness but have low strength, e.g., closed-cell plate metamaterials [21], and vice versa, the open-cell truss metamaterials have high strength with a compromise of stiffness [21]. The elusive relationship between stiffness and strength further complicates the design of mechanically robust metamaterials in water. Realizing decoupling among acoustic impedance, stiffness, and strength is expected.

This work proposes a design principle, including two steps to realize decoupling between acoustical and mechanical performance. As a proof-of-concept demonstration for the design principle, a hierarchical metamaterial with 4 times stiffer and 5 times stronger than an existing isotropic metamaterial is constructed under the same low acoustic impedance condition. The combined acoustic softness and mechanical robustness enable the hierarchical metamaterial with high transmission loss for underwater sound within low and broad frequency range. The stable acoustic performance, even under high ambient pressure, is also experimentally demonstrated.

II. DESIGN AND RESULTS

A. Two-step design principle

The first step in our design principle is utilizing anisotropy to realize decoupling between acoustic impedance and stiffness. Wave propagation in anisotropic media exhibits rich polarization characteristics absent in isotropic media [28]. These polarization characteristics simultaneously provide a chance for realizing decoupling stiffness and acoustic impedance. The effective acoustic impedance Z_e of anisotropic media is

$$Z_e = \rho_e c_{Ql} \eta, \quad (4)$$

where c_{Ql} denotes the quasilongitudinal wave-phase speed. The detailed derivation is illustrated in Note S1 within the Supplemental Material [29]. By comparing Eq. (4) with Eq. (1), an additional term η appears, which is defined as a polarization factor and is expressed by

$$\eta = \frac{c_{Qt} + c_{Ql} \tan^2 \theta_{Ql}}{c_{Ql} + c_{Ql} \tan^2 \theta_{Ql}}, \quad (5)$$

where θ_{Ql} is the polarization angle of the quasilongitudinal phase speed, i.e., the angles between the vibration direction of the material particles and the direction of the quasilongitudinal wave propagation. c_{Qt} is the quasitransverse wave phase-speed, which usually satisfies the relationship $c_{Qt} < c_{Ql}$. For isotropic media, the polarization factor η is always equivalent to 1, resulting from the purely longitudinal wave mode without polarization ($\theta_{Ql} = 0^\circ$). In contrast, the rich polarization phenomena inside anisotropic media offer the possibility of realizing a small polarization factor η . With the assistance of a polarization factor, one can realize decoupling between acoustic impedance and stiffness, i.e., to obtain a lower acoustic impedance but higher stiffness. We demonstrate that regulating the lattice orientation of the anisotropic metamaterial offers the physical realization of this counterintuitive property.

Although regulating the lattice orientation improves stiffness, it cannot ensure strength improvement for resisting yielding and failure under high ambient pressure. Due

to the nonlinear mechanic feature, decoupling strength suffers more difficulties than stiffness from the acoustic properties. The second step in the design strategy is to address this problem by learning from the architecture of biomaterials [30]. Many natural biomaterials, such as bones [31], plant stems [32], and sea sponges [33], are lightweight and strong. The common feature among these biomaterials is the hierarchical morphology of the architecture that spans multiple length scales. We introduce the hierarchical morphology into the anisotropic metamaterial and find an unprecedented decoupling property where the strength can be enhanced independently from the acoustic impedance. The strength enhancement also has little influence on the stiffness.

B. Proof-of-concept design of hierarchical metamaterial

As a proof-of-concept demonstration of the two-step design principle, the proposed underwater sound-isolation metamaterial is depicted in Fig. 1. The underwater metamaterial consists of a periodic array of lattices in the x - z plane, while the size of the metamaterial along y is assumed to be infinite. An acoustic wave is incident on the metamaterial along the $+x$ direction. Subsequently, the transmitted wave and the reflected wave are generated in the opposite direction. The primary goal of the metamaterial is to reduce the amplitude of the transmitted wave. Meanwhile, the underwater environment induces compression pressure p_0 that the metamaterial suffers. As a result, the mechanical response of the metamaterial initially displays a linear elastic stage, where the stress-strain σ - ε curve slope indicates the stiffness E . The amplitude

of compression pressure p_0 increases monotonically with water depth by $p_0 = \rho_w g h$, where ρ_w denotes the density of water, g is gravitational acceleration, and h is the water depth. Under higher compression pressure, the metamaterial suffers from large deformation and exhibits nonlinear characteristics in the σ - ε curve. A maximum stress value σ_y appears in the σ - ε curve, reflecting the metamaterial's strength. Both high stiffness and high strength are desired to obtain mechanical robustness in deep-sea environments.

Our design experiences the following iterations that gradually underpin the acoustic and mechanical performances (Fig. 2). The design process begins with a bioinspired hexagonal metamaterial denoted by design A [Fig. 2(a)], which has been demonstrated to be mechanically strong at a low density [34]. The constituent material of the lattice is chosen as a polymer resin, and the mass density is $0.25\rho_w$. The homogenization method (Note S2 within the Supplemental Material [29]) is employed to obtain the effective acoustic parameters of design A, with the results plotted on the right-hand side of Fig. 2(a). The three effective acoustic parameters, i.e., acoustic impedance \bar{Z}_e , phase speed \bar{c}_{Ql} , and polarization factor η , are presented through a relative value in the polar diagram concerning different orientations. All effective acoustic parameters appear as circles in the polar diagram, displaying isotropic characteristics. The acoustic impedance along an arbitrary direction is a constant of $0.143Z_w$, with the phase speed and polarization factor being $0.571c_w$ and 1, respectively. To lower the acoustic impedance under the same mass density value, we tune the geometric parameters based on design A (Note S3 within the Supplemental Material [29]) and obtain design B [Fig. 2(b)]. Different from design A, the acoustic impedance (green

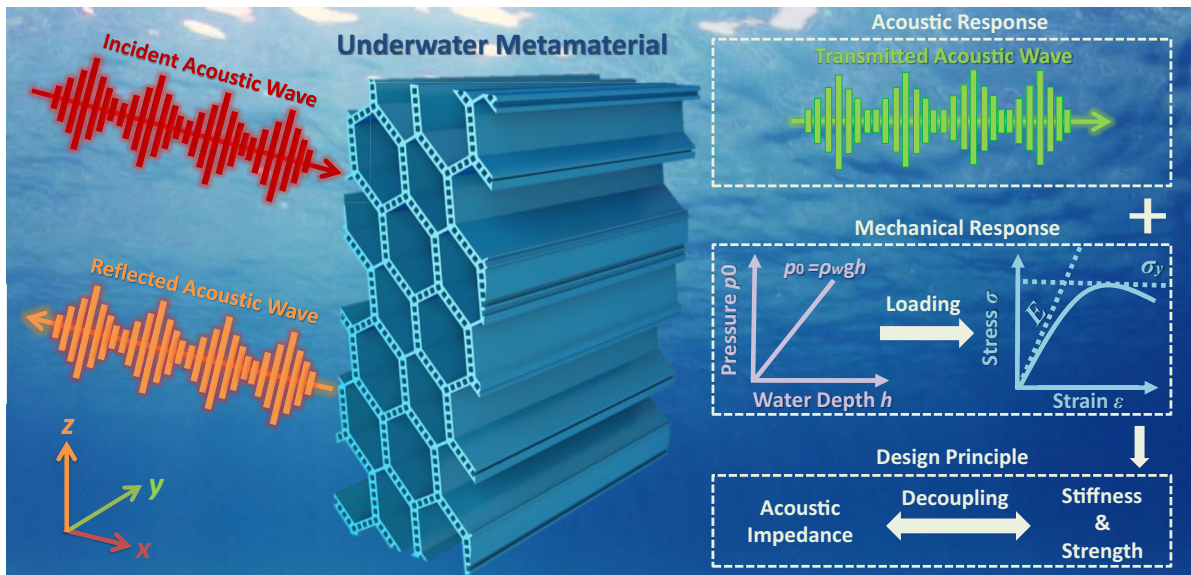


FIG. 1. Conceptual graph of the metamaterial with application to underwater sound isolation.

line) in the polar diagram displays a peanutlike pattern and anisotropic characteristics. Along the x direction, the acoustic impedance is lowered to $0.0798 Z_w$ and almost half that of design A. The lower acoustic impedance results from the slower phase speed ($0.319c_w$), while the polarization factor η remains unity. However, following the observation of the smaller polarization factor along the other orientation, we regulate the lattice orientation of design B through anticlockwise rotation by an angle of $\gamma = 26^\circ$, with the obtained configuration denoted by design C. The effective acoustic parameters of design C are depicted via the purple line in the same polar diagram of design B for intuitive comparison. The acoustic impedance along the x direction is further reduced to $0.0668Z_w$. Compared with design B, the lower acoustic impedance is mainly attributed to design C obtaining a smaller polarization factor (0.553), while it even possesses a higher phase speed ($0.483c_w$), implying that achieving a smaller polarization factor is the key to lowering the acoustic impedance. Last, the architecture of bones also gives us an essential

inspiration for the design. As shown in Fig. 2(c), the bones consist of two structural hierarchies. The first-order structural hierarchy, i.e., the outer scaffold, consists of stiff *cortical bone*, while the *trabecular bone*, which is one order of magnitude smaller than *cortical bone*, forms the second-order structural hierarchy and occupies the scaffold [31]. Wolff's law [35] can well elucidate this architecture. During the evolution process in nature, closed outer shells and internal structures are adapted to ensure the mechanical robustness of bones concerning external force variations, thus resulting in the hierarchical architecture. Motivated by bones' architectures, we elaborately introduce hierarchical morphology into the metamaterial and construct design D [Fig. 2(d)]. The first-order structural hierarchy for design D still keeps the hexagonal shape, the same as design C. However, in contrast to the members of design C formed by fully dense solids, those of design D consist of square lattices [36] as the second-order structural hierarchy. The square lattice brings design freedom, i.e., the infill porosity \bar{P} of the members, which is defined as

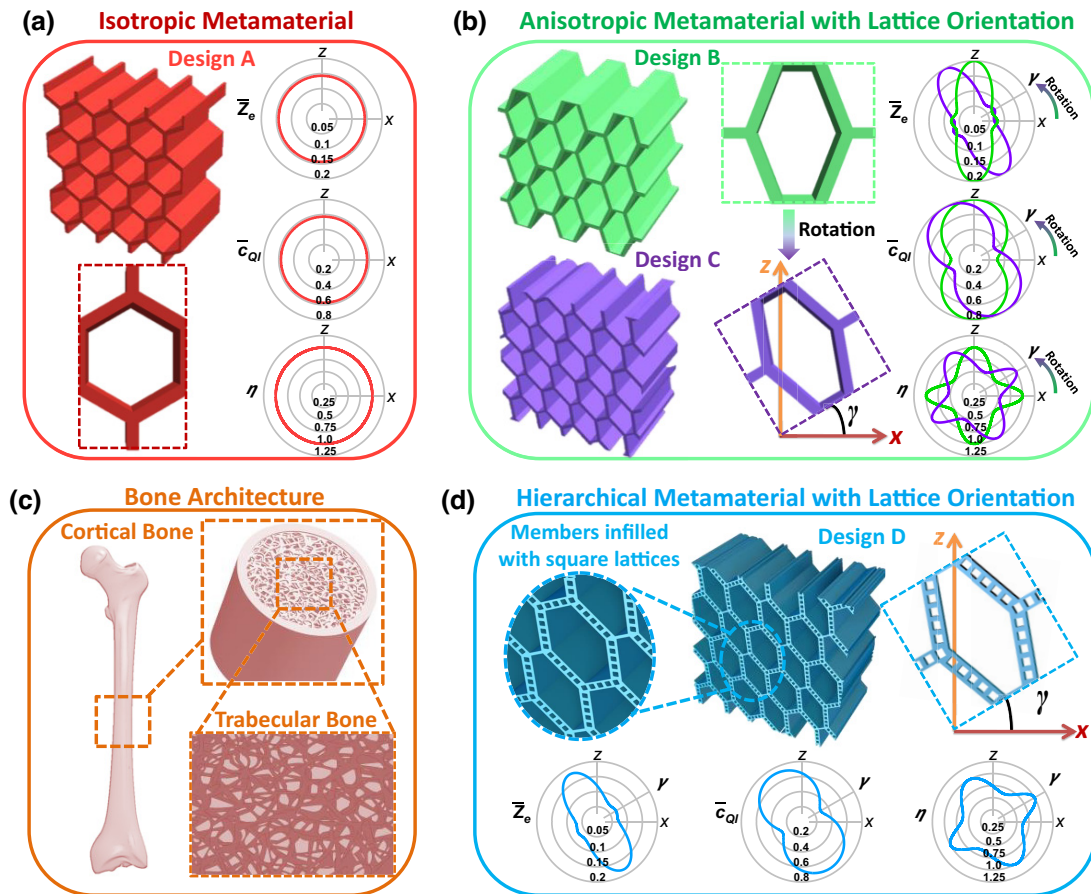


FIG. 2. Illustration of the design process for underwater hierarchical metamaterials. (a),(b) Schematic diagrams of designs A (a), B, and C (b). At the right hand of each diagram, the effective acoustic parameters of each design are displayed in a polar diagram concerning different orientations, where the color is consistent with those of sketch maps of designs. The number marked in the polarization diagram represents the value of each contour (gray line). Dividing the values of acoustic impedance $Z_w = 1.5 \times 10^6 \text{Pa s/m}$ and the longitudinal wave phase speed $c_w = 1500 \text{ m/s}$ of water, \bar{Z}_e and \bar{c}_{ql} denote the each design's relative acoustic impedance and relative longitudinal wave-phase speed. (c) Sketch of the architecture of the bone. (d) Schematic diagrams of design D, where the effective acoustic parameters are displayed on the bottom.

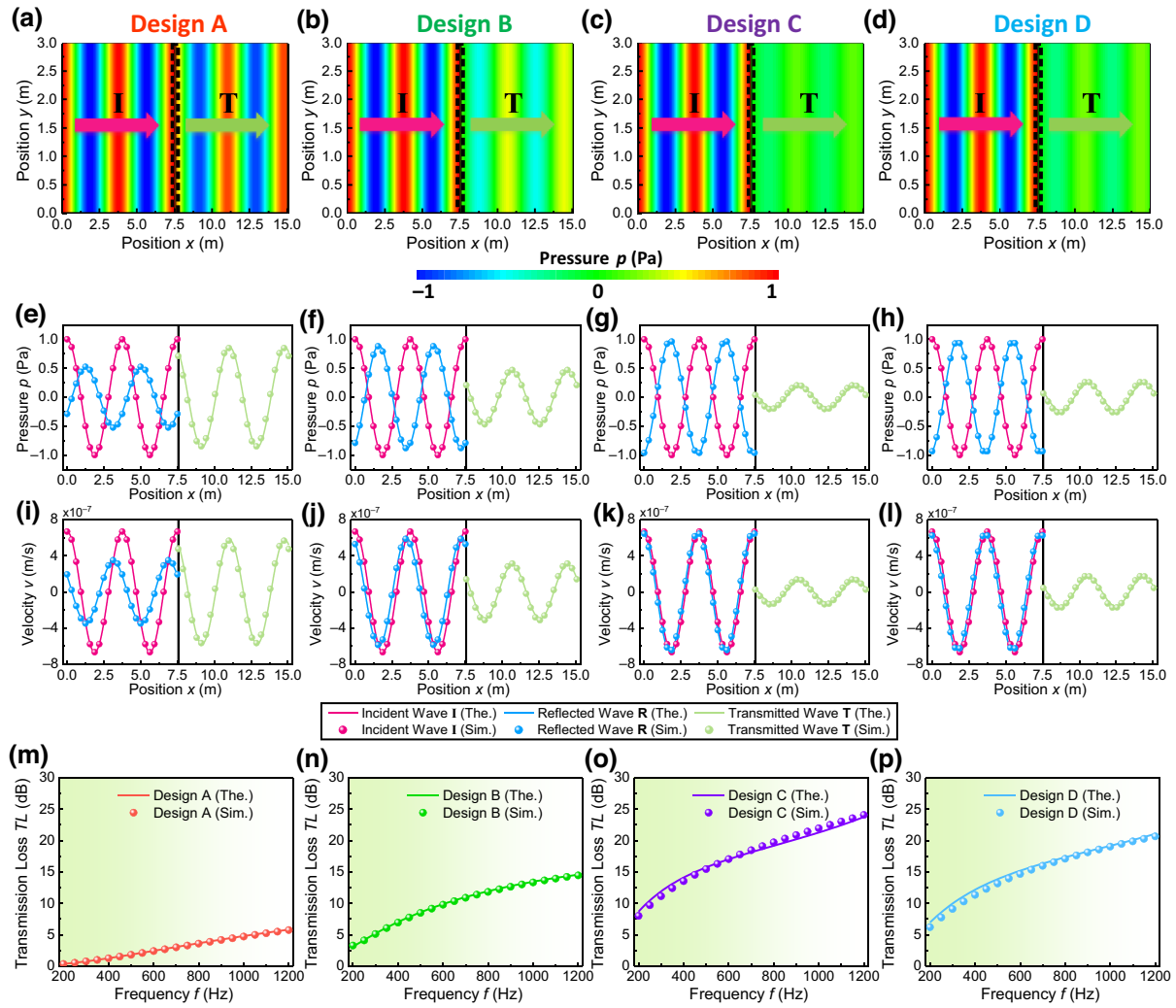


FIG. 3. Acoustical performance of designs A–D. (a)–(d) Theoretical predictions of acoustic pressure patterns for designs A–D under the condition of an incident plane wave with a frequency of 400 Hz. The marks **I** and **T** denote the incidence and transmission, respectively. The arrows indicate the wave propagation direction. (e)–(h) Profiles of the acoustic pressure for designs A (e), B (f), C (g), and D (h). (i)–(l) Profiles of the particle velocity for designs A (i), B (j), C (k), and D (l). In plots (e)–(l), the solid lines and circles denote the theoretical and numerical results, respectively. The results for incidence **I**, reflectance **R**, and transmittance **T** are color coded by red, blue, and green, respectively. (m)–(p) Acoustic transmission loss as a function of frequency for designs A (m), B (n), C (o), and D (p), where the solid lines and circles are results obtained by theory (Note S4 within the Supplemental Material [29]) and simulation (Note S5 within the Supplemental Material [29]), respectively.

the ratio of the volume of square hollows to all members. The three effective acoustic parameters of design D with $\bar{P} = 35\%$ are displayed on the bottom side of Fig. 1(d). The three patterns show shapes similar to those of design C, implying that the second-order structural hierarchy hardly affects the acoustic properties. The acoustic impedance of design D reaches $0.0683Z_w$ and is slightly higher than that of design C.

C. Acoustical performance of metamaterials in water

To prove the effectiveness of our design principles with underwater sound isolation, a frequency-domain model

based on acoustic-solid interaction theory is established (Note S4 within the Supplemental Material [29]). To acquire an intuitive understanding, Figs. 3(a)–3(d) depict the acoustic pressure patterns of designs A–D. A plane acoustic wave with a frequency of 400 Hz and amplitude of 1 Pa is generated at the position of $x = 0$ m. The incident direction is along the $+x$ direction. The acoustic wave front along the z direction is assumed to be a constant. The metamaterial with a thickness of 54 mm (marked by a black dashed box) is placed at the position of $x = 7.5$ m. There is a cover layer consisting of homogenous polymer resin, with a thickness of 2 mm, between the lattice material and the surrounding water on both sides. The left and

right patterns of the metamaterial represent the incident wave (denoted by **I**) and transmitted wave (denoted by **T**), respectively. For design A, the transmitted wave shows almost the same pattern as the incident wave, implying that design A can be treated to be transparent to incident wave **I**. Regarding design B, one can readily see that more acoustic waves are blocked due to a lower acoustic impedance than in design A. With further regulating lattice orientation, there is a stark difference between the incident and transmission ends for designs C and D. The transmission ends display a “dark” region through which near-zero acoustic energy can pass.

The profiles of acoustic pressure and velocity fields along the propagating direction are illustrated in Figs. 3(e)–3(l). The red, blue, and green lines denote the incident, reflected, and transmitted waves, respectively. The numerical simulations are conducted to validate our theoretical model, with the results shown by circles. Overall, the two results agree well with each other, demonstrating the accuracy of the theoretical model. For designs C and D, in addition to featuring small amplitudes for transmitted wave **T**, it is also noted that there is a phase change in π between incident wave **I** and reflected wave **R** for the pressure field. In contrast, the velocity field of the reflected wave **R** is in phase with that of incident wave **I**. The combination of these characteristics further corroborates that both designs can be treated as acoustically soft boundaries [37] in water.

Owing to the nonresonance characteristic in the low-frequency domain, designs C and D possess a broad working bandwidth rather than only being effective at a single frequency. Figures 3(m)–3(p) plot the transmission loss TL as a function of frequency f . The TL is defined by $TL = -20 \log_{10} |P_t/P_i|$, where P_t and P_i denote the magnitude of the pressure of the transmitted and incident wave. In the extremely low and broad frequency range from 200 to 1200 Hz, both designs C and D display high TL without apparent fluctuation. The average TL for the two designs, respectively, reaches 17.9 and 15.8 dB, meaning that over 95% acoustic energy is reflected. In contrast, designs A and B show average TL of 3.0 and 10.1 dB. This comparison highlights the role of low acoustic impedance in isolating underwater sound in the low-frequency range. Even under oblique incidence and diffuse field, designs C and D still maintain high TL and outperform the other designs (Note S6 within the Supplemental Material [29]). Moreover, designs C and D possess deep-subwavelength thicknesses with only 1/129 of the operating wavelength. The deep-subwavelength thickness is appealing for some application scenarios where the space is also limited.

D. Mechanical performance of metamaterials

In addition to the low acoustic impedance for sound isolation, robust mechanical properties are required

for the metamaterial to withstand naturally occurring compression pressure in underwater environments. Computational modeling (Note S5 within the Supplemental Material [29]) combined with the experimental method (Note S9 within the Supplemental Material [29]) is carried out to assess the uniaxial compression response of the metamaterials, with results presented in Fig. 4. Figures 4(a) and 4(b) depict the stress-strain curves of the four metamaterials obtained by the two methods. All stress-strain curves initially show a linear region. As the strain increases, yielding occurs inside the metamaterial, leading to a gradual reduction in stiffness and a maximum value for stress. Subsequently, the metamaterial shows near-zero or negative stiffness until a fracture occurs, which is reflected by the sudden drop in stress. In general, the results predicted by simulations show agreement with the experimental results, validating the accuracy of experimental measurements in capturing the linear elastic region and the maximum load-bearing capability. By comparing the experimentally obtained stress-strain curves among the four designs, three features are noteworthy: (i) design A is characterized by both the highest initial stiffness (42.69 MPa) and strength (2.35 MPa), whereas design B is the worst-performing design regarding the stiffness (12.90 MPa) and strength (1.10 MPa). (ii) Sharing the same topology but different lattice orientations with design B, design C acquires a higher initial stiffness (22.59 MPa), demonstrating that the lattice orientation modulation can improve the initial stiffness. However, despite having a higher stiffness, the strength of design C (1.29 MPa) is comparable to that of design B. (iii) By comparing designs C and D, the two show a similar initial stiffness but distinctive strength. A higher strength (2.13 MPa) for design D is a possible result of incorporating hierarchical morphology.

Figures 4(c) and 4(d) further compare the snapshots of undeformed specimens with deformed specimens in the vicinity of the maximum stress. The von Mises stress distributions obtained from simulations are displayed in Fig. 4(e) to assist in the understanding of deformation behaviors. Design A shows a relatively global deformation mode where compression along the x direction leads to a flattening of the lattice. The oblique members of the metamaterial spread out and undergo rotation around their nodes. The rotation of the members also results in nonlinear mechanical behavior, which is reflected by the gradual stiffness reduction in the stress-strain curve. For design B, the obtuse angle between the two oblique members and the shorter vertical members results in fewer materials distributed along the loading direction. Therefore, design B shows a low initial stiffness. Upon loading, the oblique members carry the most loads and rotate about the nodes, giving rise to the horizontal elongation of the lattice. However, the vertical members undergo minimal stretch deformation and are inefficient in transmitting the loads among each layer. As a result, design B is prone

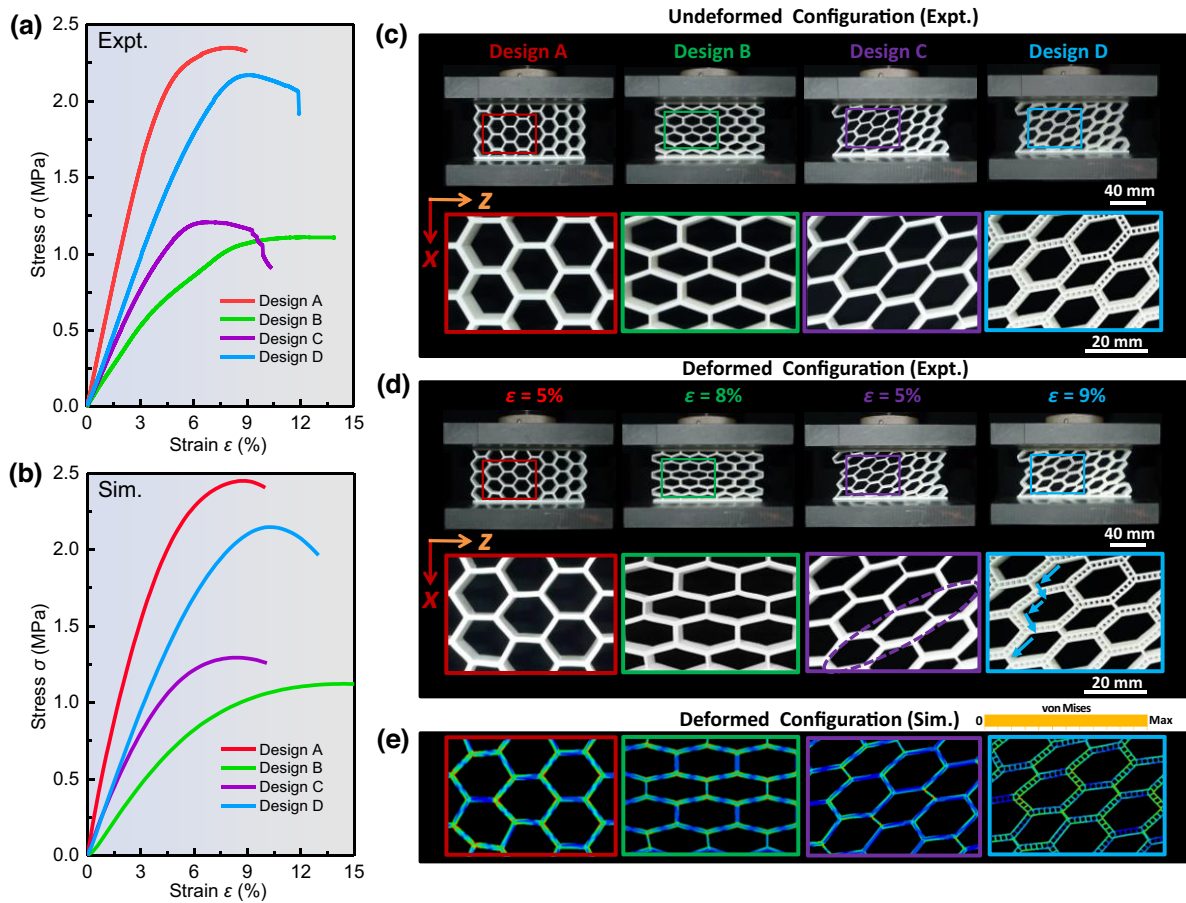


FIG. 4. Uniaxial compression performances of the metamaterials. (a),(b) Stress-strain curves of the metamaterials obtained by experiments (a) and finite-element simulations (b). (c),(d) Snapshots of designs A–D during the uniaxial compression experiments. The undeformed configurations (0% applied strain) are plotted in (c), while the deformed configurations around maximum stress are given in (d). In both (c),(d), the closeup of the local configuration inside the dashed box is presented at the bottom; scale bars for snapshots in the first and second rows are 40 and 20 mm. In (d), the applied strains for designs A–D are 5, 8, 5, and 9%, respectively. (e) Simulated results of the deformed patterns for designs A–D with von Mises stress distribution. The applied strains for designs A–D are 5, 8, 5, and 9%, respectively. The color bar denotes the stress level inside the materials.

to suffer localized stress concentrations in the vicinity of nodes that weaken the load-bearing capability. By regulating the lattice orientation, more materials inside design C are distributed near the loading direction than in design B, resulting in a higher initial stiffness. Nevertheless, the change in orientation of the lattice induces a mechanical maximum shear stress plane when it suffers vertical loads. As highlighted by a purple dashed line in Fig. 4(d), the nodes inside this plane experience shear force from the compression loads, and the members outside the plane exhibit minimal deformation. These extremely localized shear transformation zones form a slip band, similar to the slip activity in single crystals [38]. Due to the emergence of a localized slip band, design C exhibits a severely uneven stress distribution and high stress concentration. Hence, although design C acquires a higher initial stiffness, its maximum load-bearing capability is comparable to

that of design B. Thus far, the regulating lattice orientation is sweet and sour. It is sweet because regulating the lattice orientation is crucial for lowering the acoustic impedance while simultaneously improving the initial stiffness. However, it is sour as a consequence of inducing a maximum shear stress plane that forms the slip band, leading to little improvement in strength. Incorporating a hierarchical morphology offers a promising path to overcome the detrimental effect on strength from the slip band. By comparing designs C with D, computational modeling and experimental observation demonstrate that integrating the hierarchical morphology induces a transition from a highly localized deformation mode into a relatively global mode. The deformation of design D is mainly governed by the bending of the members consisting of square lattices, which shows a high-order buckling mode in the vicinity of the maximum stress. Meanwhile,

the square lattices inside the members enhance the overall deformation compatibility of the network and promote load transfer between the adjacent members (indicated by blue arrows). Figure 4(e) shows that design D displays a more even stress distribution than design C, thereby delaying the yielding point.

E. Acoustic mechanical decoupling property enabled by the design principle

Underwater metamaterials with application to sound isolation require low acoustic impedance and mechanical robustness simultaneously, which are two mutually exclusive properties for common materials in nature. The pursuit of design principles with the ability to realize decoupling between mechanical properties and acoustical characteristics is therefore highly desirable. We next demonstrate the generality of our design principle in this context. Figures 5(a)–5(c) compare the acoustic impedance \bar{Z} , compression modulus \bar{E} , and strength $\bar{\sigma}$ variation with the relative density $\bar{\rho}$ for designs A–D. The lattice orientations for designs C and D are kept constant at $\gamma = 26^\circ$, while the infill porosity of members for the latter is fixed at $\bar{P} = 35\%$ with different densities $\bar{\rho}$. The dashed lines denote the fit curve in the form of a power law, where the proportionality constant and the scaling exponent are presented in brackets. As depicted in Fig. 5(a), the impedance of designs A and B show a linear scaling relationship with the density, i.e., $\bar{Z} \sim \bar{\rho}$. Design B acquires a smaller proportionality constant and nearly half the impedance of design A under the same density, stemming from the lower longitudinal phase speed. However, the stiffness and the strength of design B are approximately only 1/3 and 1/2 of those of design A, respectively. The comparison between the two designs indicates a general trade-off challenge that materials have experienced between low acoustic impedance and high mechanical properties. The lattice orientation regulation offers a promising path to overcome the trade-off between acoustic impedance and stiffness. A steeper scaling relationship, i.e., $\bar{Z} \sim \bar{\rho}^{1.6}$, is achieved for both designs C and D, enabling them to acquire a lower acoustic impedance than the other two designs. The larger scaling exponent in acoustic impedance mainly results from the lower polarization factor acquired by the lattice orientation regulation. Meanwhile, the material distribution is also changed in a positive sense toward higher initial stiffness. As reflected in Fig. 5(b), design C is 1.6 to 1.75 times stiffer than design B under the same density. However, even though design C has a higher initial stiffness, the lattice orientation regulation cannot contribute to the strength enhancement [Fig. 5(c)], because it induces localized shear transformation zones where the slip band of high-stress forms. Incorporating hierarchical morphology is an effective strategy for overcoming this problem. By

comparing the strength between designs C and D, one can see that the latter is 1.5 to 1.7 times as strong as the former at the same density.

Design D with a hierarchical morphology possesses additional design freedom than other designs, i.e., the infill porosity \bar{P} for the square lattice inside the members. To fully identify its effects, Figs. 5(d)–5(f) illustrate the acoustic and mechanical properties of design D versus the combination of relative density $\bar{\rho}$ and infill porosity \bar{P} . In a sense, design C can be treated as a particular case of design D with infill porosity $\bar{P} = 0\%$. Under each density, one can see from Fig. 5(d) that the acoustic impedance is insensitive to the variation in infill porosity and almost remains constant. However, when the infill porosity \bar{P} is raised, gentle stiffness improvement and noticeable strength enhancement are observed in Figs. 5(e) and 5(f), respectively. The combination of Figs. 5(d)–5(f) displays an unprecedented decoupling characteristic between the acoustical and mechanical properties. We exemplify the acoustic transmission loss and uniaxial compression response of four designs with the same relative density $\bar{\rho} = 25\%$ yet different infill porosities \bar{P} , as shown in Figs. 5(g) and 5(h). The four designs exhibit nearly indistinguishable acoustic transmission loss, in which the average TL achieves over 15 dB in the low-frequency range from 200 to 1200 Hz. However, raising the infill porosity results in a distinct mechanical behavior [Fig. 5(h)], i.e., although the initial stiffness only shows a gentle increase, a noticeable enhancement in the maximum load-bearing ability is observed.

We then attempt to uncover the origin of this strength enhancement by comparing the deformation mode and stress distribution [Fig. 5(i)]. The following reasons can interpret the strength enhancement. On the one hand, the failure of design D with low infill porosity is primarily triggered by the formation of a localized slip band of high-stress concentration, however, enhancing the infill porosity could induce a transition from a highly localized mode into a relatively global mode. When the infill porosity is increased, the square hollows split the members into finer networks that can provide multiple transmission paths for loads. Therefore, the hierarchical members consisting of square lattices play a more critical role in load carrying. The enhanced bending behavior of hierarchical members acts as bridges to efficiently deliver loads and enables a more uniform stress distribution than that with lower infill porosity. The more compatible deformation among the interconnected members alleviates the formation of localized shear transformation zones that induce the slip band. On the other hand, the high-order buckling of the hierarchical member dominates the failure of design D with higher infill porosity. Increasing the infill porosity enhances the effective width-to-length ratio of the hierarchical members, and offers a higher bending strength for the member to resist buckling.

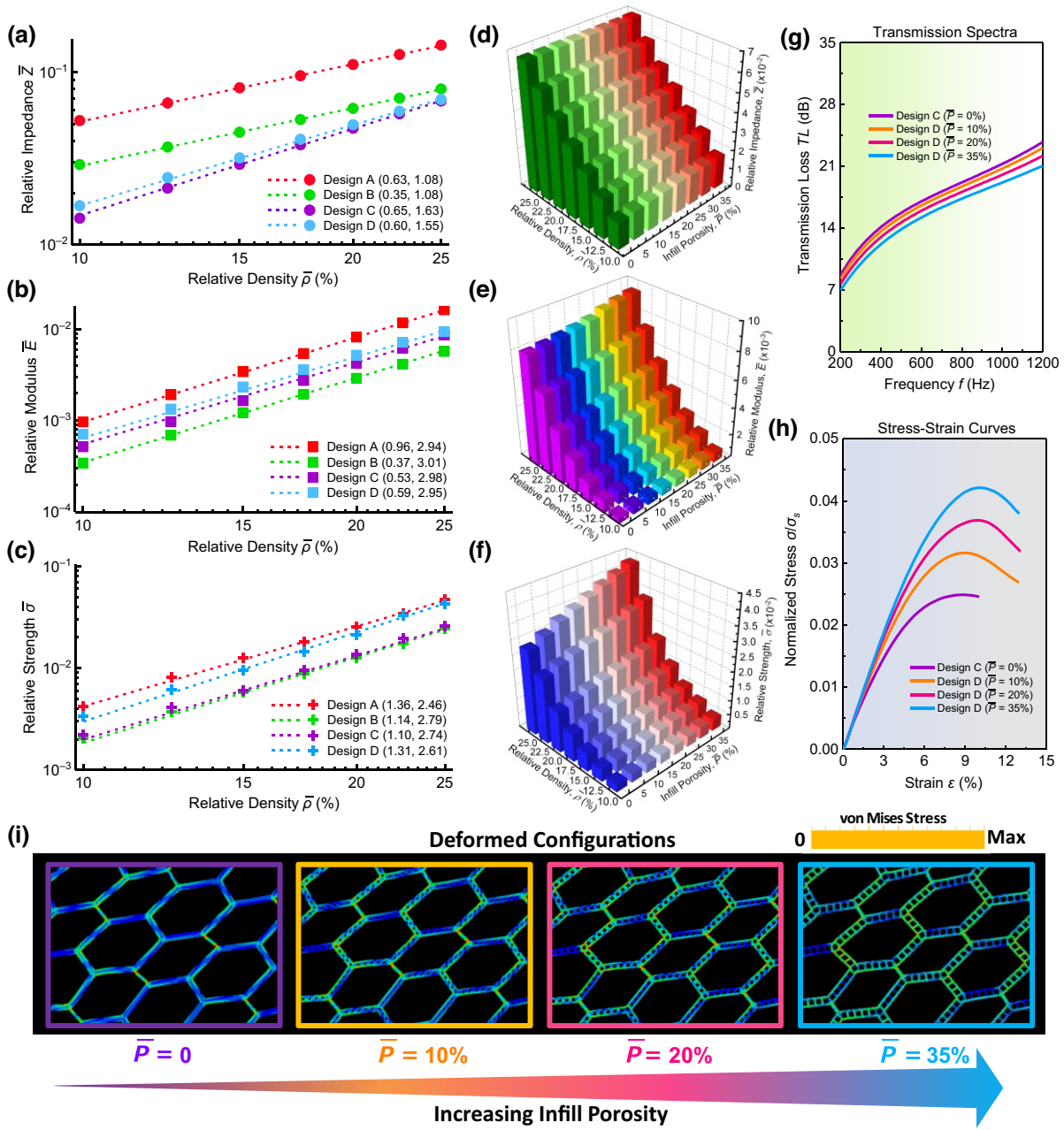


FIG. 5. Illustration of the acoustic mechanical decoupling property enabled by the design principle. (a)–(c) Relative acoustic impedance (a), stiffness (b), and strength (c) plotted against density for designs A–D. Here, the relative acoustic impedance \bar{Z} and density $\bar{\rho}$ are values normalized by those of water, while the relative stiffness \bar{E} and strength $\bar{\sigma}$ are normalized by Young’s modulus E_s and yield strength σ_s of the constituent material. (d)–(f) Relative acoustic impedance (d), stiffness (e), and strength (f) correspond to design D with simultaneously varying density $\bar{\rho}$ and infill porosity \bar{P} . (g), (h) Transmission loss in water (g) and stress-strain curves under uniaxial compression (h) of design D with the same density $\bar{\rho} = 25\%$ but different infill porosities \bar{P} . Stress distributions of design D with different infill porosities are shown in (i). The color bar on the top denotes the inside stress level.

F. Robust underwater sound isolation under high ambient pressure

Having shown that our design principle endows the metamaterial with a combination of acoustically soft and mechanically robust properties, we further experimentally demonstrate robust underwater sound isolation under high

ambient pressure. To this end, a water-filled impedance tube with a two-load transfer function method (Note S10 within the Supplemental Material [29]) is employed to obtain the acoustic response of the specimens. The sketch and photos of the experimental setup are displayed in Figs. 6(a) and 6(b), respectively. The cylindrical

impedance tube consists of stainless steel with dimensions of 6000 mm (length) by 120 mm (inner diameter), and the wall thickness is 100 mm. A transducer is mounted at one end of the tube to generate acoustic waves. At the other end of the tube, each test includes two basic measurements with different terminations, i.e., an anechoic termination formed by three absorbing wedges with thicknesses of 350 mm to absorb outgoing waves and a reflective termination consisting of an air tube with a thickness of 500 mm. Four hydrophones are placed inside the tube wall to sense the acoustic pressure in water. The specimen is positioned in the middle part of the tube. The impedance tube is connected to an external nitrogen pump via a pipeline to emulate the deep-water environment with static ambient pressure. The amplitude of static ambient pressure inside the impedance tube can be monitored by the manometer and tuned through the valve. After each hydrophone obtains the acoustic pressure signal, 1000 transfer functions between hydrophones are obtained and averaged in the frequency domain. The sound transmission loss TL is finally used to characterize the sound isolation performance of the specimen. The frequency range for measurement is between 400 and 1200 Hz with an interval of 50 Hz. The ambient pressures inside the impedance tube for each test are chosen as 0.1, 0.5, 1, 1.5, and 2 MPa, simulating the pressure environment from shallow water (approximately 10 m) to deep water (approximately 200 m).

We first test the TL of four specimens corresponding to designs A–D, with the results depicted in Figs. 6(d)–6(h), respectively. The four specimens have the same density value of $\bar{\rho} = 25\%$, while the infill porosity for design D is $\bar{P} = 35\%$. Under atmospheric pressure ($p_0 = 0.1$ MPa), the measured TL of the four designs [Fig. 6(d)] show agreement with the results obtained by the theory [Fig. 6(c)]. The observable discrepancies may stem from the following two aspects: (i) the inevitable errors in manufacturing processing result in the imperfection of geometric size and roughness of the surface; and (ii) the measurement errors from the hydrophones when receiving pressure signals lead to a fluctuation in the data. The TL of design C compares well with that of design D, with the average value reaching 17.4 and 16.8 dB in the low-frequency range from 400 to 1200 Hz, respectively. In contrast, designs A and B have average TL of 3.8 and 11.1 dB. Under moderate ambient pressures of 0.5 [Fig. 6(e)] and 1 MPa [Fig. 6(f)], four specimens exhibit slight decreases in TL compared with the atmospheric pressure condition, but the average TL of designs C and D remain at a high value over 13 dB under a pressure of 1 MPa. When the ambient pressure is further increased to a higher level of 1.5 MPa, catastrophic failure occurs for designs B and C in the impedance tube, as a result of which the external pressure exceeds the maximum load-bearing capability. This again illustrates that the metamaterial with high initial stiffness can only maintain

robust acoustic performance under pressure conditions in linear elastic regions. To work in the higher ambient pressure, high strength should be highlighted. Both designs A and D with superior strength demonstrate this point. Even under high ambient pressure of 2 MPa, the two designs are robust in the water-filled impedance tube. Design D still displays an average TL over 10 dB, while this value for design A is only 2.1 dB due to the higher acoustic impedance.

Under the premise of the same density $\bar{\rho} = 25\%$, although design D outperforms design A in underwater sound isolation, it possesses slightly inferior mechanical performance. For a more convincing comparison, an additional control experiment is carried out for design A with a lower density $\bar{\rho} = 12\%$. The reduction in density leads to a higher TL , where the average value is increased to 14.2 dB under atmospheric pressure [Fig. 6(i)]. However, acquiring a comparable acoustic performance to that of design D severely degrades the mechanical performance [Fig. 6(j)]. Young's modulus (4.62 MPa) and the strength (0.375 MPa) are approximately 1/5 and 1/6 those of design D, respectively. This comparison further demonstrates that our design principle enables the metamaterial to have an unprecedented combination of low acoustic impedance and mechanical robustness.

III. FURTHER DISCUSSIONS

Figures 5(b) and 5(c) reveal that the modulus and strength scaling exponents versus the density for designs A–D range from 2 to 3, implying bending-dominated behavior upon loading. With a constraint on the density, mechanical performance competitions over the past few decades have shown that bending-dominated lattices are inferior to their stretching-dominated counterparts [39–41]. Nevertheless, when the constraint is changed from density to acoustic property, are the stretching-dominated lattices still the winner of the mechanical competition? To answer this question, we launch another competition among the proposed designs and six well-known stretching-dominated lattices [33,36,39,41], whose configurations are depicted in Fig. 7(a). Among the stretching-dominated lattices, the modulus of the square lattice has been demonstrated to be close to the Hashin-Shtrikman bounds within a given density [42]. Motivated by the hierarchical skeleton of the deep-sea sponge *Euplectella* sp. [43] the sponge-inspired lattice shows excellent strength [33]. However, these stretching-dominated lattices have more difficulty obtaining low acoustic impedance than our proposed designs. Within a density of $\bar{\rho} = 25\%$, these materials are almost acoustically transparent to underwater sound and display low TL with an average value of less than 2 dB in the low-frequency range from 200 to 1200 Hz (Note S11 within the Supplemental Material [29]). To

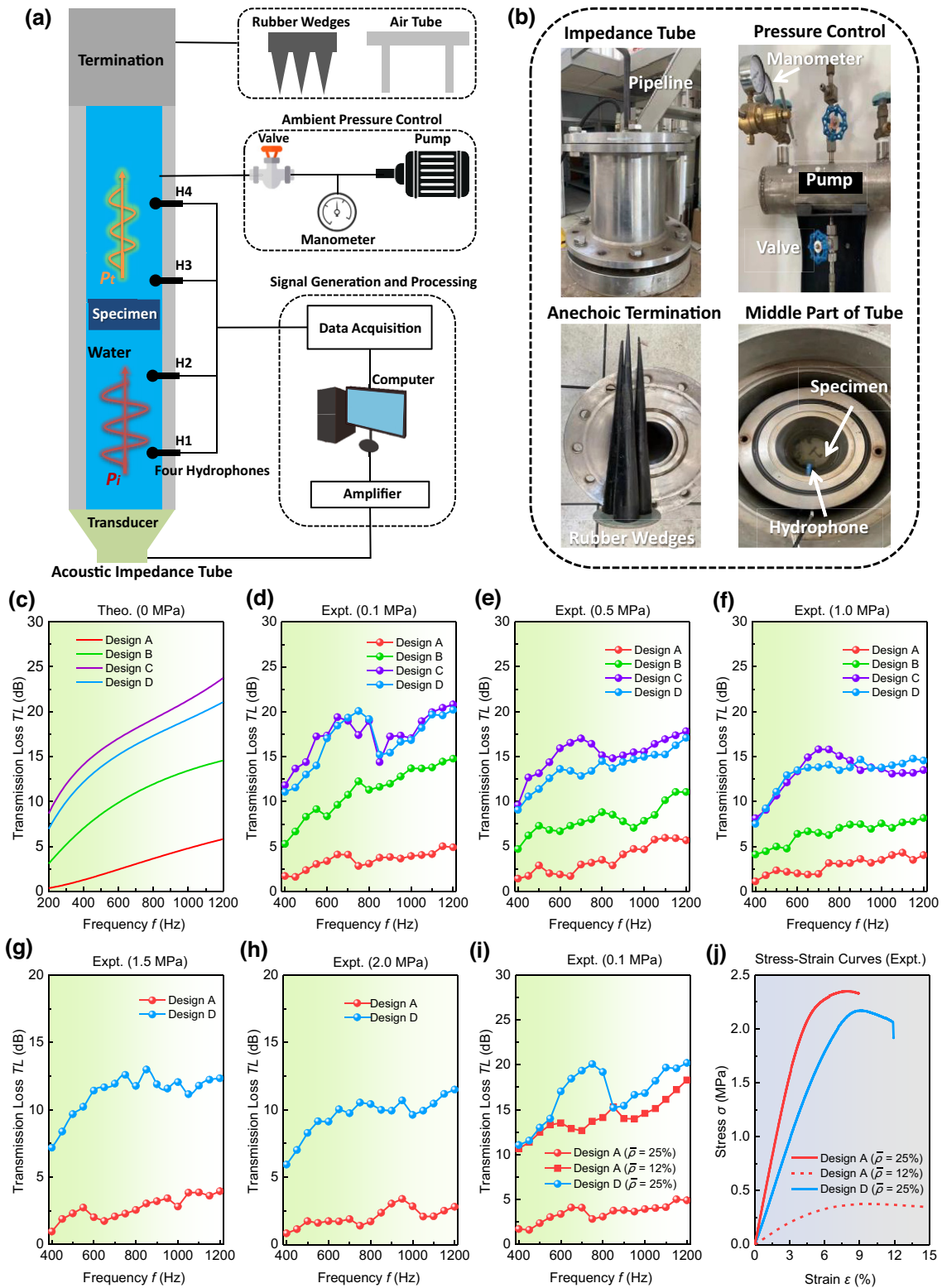


FIG. 6. Illustrations of the setup and results of the hydroacoustic experiment. Schematic diagram (a) and photos (b) of the experimental setup. (c) Theoretical prediction for the TL of specimens with a density value $\bar{\rho} = 25\%$. (d)–(h) Experimental results for the TL of specimens within ambient pressure values of $p_0 = 0.1$ MPa (d), $p_0 = 0.5$ MPa (e), $p_0 = 1.0$ MPa (f), $p_0 = 1.5$ MPa (g), and $p_0 = 2.0$ MPa (h). (i),(j) To ensure a fairer comparison between designs A and D, the density value of design A is reduced to $\bar{\rho} = 12\%$, with the hydroacoustic experiment results given in (i). The comparison of the stress-strain curves is plotted in (j) to illustrate the compromise of the mechanical performance with decreasing density.

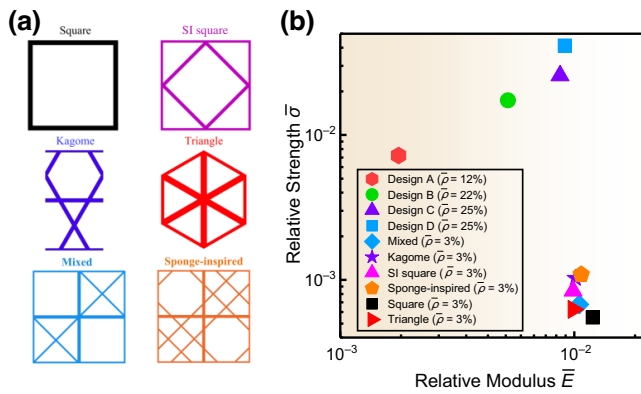


FIG. 7. Mechanical competitions within constraints on acoustic impedance. (a) Configurations of the existing stretching-dominated lattices in the literatures with square, SI square, kagome, triangular, mixed, and sponge-inspired shapes. (b) Compression stiffness and strength performance competitions among designs A–D and stretching-dominated lattices to obtain comparable TL .

acquire a similar TL to design D with $\bar{\rho} = 25\%$, the density should be reduced to $\bar{\rho} = 3\%$ (Note S11 within the Supplemental Material [29]). Nevertheless, the reduction in density severely comes at the price of their mechanical performance. Although the stretching-dominated lattices possess a comparable initial modulus, their strength is lower by more than an order of magnitude than that of design D [Fig. 7(b)]. It again emphasizes that a high stiffness cannot ensure a high strength. The extremely low strength implies that the low-density stretching-dominated lattices suffer structural collapse and failure, even under a small ambient pressure, hindering their application in natural marine environments.

IV. CONCLUSIONS

In summary, this work proposes a design principle to overcome the mutual exclusion of low acoustic impedance and high mechanical properties in the existing materials. The design principle includes two steps that regulate the lattice orientation and incorporate a hierarchical morphology in an anisotropic metamaterial. Regulating the lattice orientation triggers the polarization of the wave propagation in the anisotropic metamaterial, leading to a lower acoustic impedance. Meanwhile, the lattice orientation regulation changes the material’s distribution, contributing to the initial stiffness improvement. By mimicking the architecture of the bone and incorporating a hierarchical morphology, an unprecedented decoupling between acoustic and mechanical properties is obtained for metamaterials to enhance strength independently from the acoustic impedance. The strength enhancement stems from combining local hierarchical members, the promotion of global deformation compatibility, and efficient load

delivery throughout the network. As a proof-of-concept demonstration, a hierarchical metamaterial with 4 times higher stiffness and 5 times higher strength than the existing isotropic metamaterial is constructed under the same low acoustic impedance. The hierarchical metamaterial could represent a promising candidate for underwater sound isolation, which displays high sound transmission loss in an extremely low and broad frequency range. More critical for practical applications, the hierarchical metamaterial can maintain robust acoustic performance even under high ambient pressure. In addition to the application for underwater noise control, from a higher perspective, our design principle opens an alternative avenue for engineering metamaterials combining mutually antagonistic functional properties.

ACKNOWLEDGMENTS

This work was supported by the National Natural Science Foundation of China (Grants No. 11991032, No. 52171327, and No. 51805537). The authors would like to thank Mr Xiaowei Zhang (National Key Laboratory on Ship Vibration and Noise, Wuxi, Jiangsu, China) for his help in the experiment.

- [1] K. Robert, Deep-sea biology: Living with the endless frontier, *Science* **302**, 991 (2003).
- [2] W. Wang, C. Hu, J. Ni, Y. Ding, J. Weng, B. Liang, C.-W. Qiu, and J.-C. Cheng, Efficient and high-purity sound frequency conversion with a passive linear metasurface, *Adv. Sci.* **9**, 2203482 (2022).
- [3] K. Wu, J. Liu, Y.-J. Ding, W. Wang, B. Liang, and J.-C. Cheng, Metamaterial-based real-time communication with high information density by multipath twisting of acoustic wave, *Nat. Commun.* **13**, 5171 (2022).
- [4] S. Qu, N. Gao, A. Tinel, B. Morvan, V. Romero-García, J. P. Groby, and P. Sheng, Underwater metamaterial absorber with impedance-matched composite, *Sci. Adv.* **8**, abm4206 (2022).
- [5] V. Leroy, A. Strybulevych, M. Lanoy, F. Lemoultet, A. Tourin, and J. H. Page, Superabsorption of acoustic waves with bubble metascreens, *Phys. Rev. B* **91**, 020301(R) (2015).
- [6] Z. Huang, S. D. Zhao, M. Su, Q. Yang, L. Zheng, Z. Cai, H. Zhao, X. Hu, H. Zhou, F. Li, J. Yang, Y.-S. Wang, and Y. Song, Bioinspired patterned bubbles for broad and low-frequency acoustic blocking, *ACS Appl. Mater. Interfaces* **12**, 1757 (2020).
- [7] Y. Chen, B. Zhao, X. Liu, and G. Hu, Highly anisotropic hexagonal lattice material for low frequency water sound insulation, *Extreme Mech. Lett.* **40**, 100916 (2020).
- [8] H. Yang, Y. Xiao, H. Zhao, J. Zhong, and J. Wen, On wave propagation and attenuation properties of underwater acoustic screens consisting of periodically perforated rubber layers with metal plates, *J. Sound. Vib.* **444**, 21 (2019).

- [9] Y. Wang, H. Zhao, H. Yang, J. Liu, D. Yu, and J. Wen, Topological design of lattice materials with application to underwater sound insulation, *Mech. Syst. Signal Process.* **171**, 108911 (2022).
- [10] D. C. Calvo, A. Thangawng, C. N. Layman, R. Casalini, and S. Othman, Underwater sound transmission through arrays of disk cavities in a soft elastic medium, *J. Acoust. Soc. Am.* **138**, 2537 (2015).
- [11] K. Zhang, C. Ma, Q. He, S. Lin, Y. Chen, Y. Zhang, N. Fang, and X. Zhao, Metagel with broadband tunable acoustic properties over air-water-solid ranges, *Adv. Funct. Mater.* **29**, 1903699 (2019).
- [12] B. Zhao, D. Wang, P. Zhou, X. Liu, and G. Hu, Design of load-bearing materials for isolation of low-frequency waterborne sound, *Phys. Rev. Appl.* **17**, 034065 (2022).
- [13] Z. Cai, S. Zhao, Z. Huang, L. Zheng, M. Su, Z. Zhang, Z. Zhao, X. Hu, Y.-S. Wang, and Y. Song, Bubble architectures for locally resonant acoustic metamaterials, *Adv. Funct. Mater.* **29**, 1906984 (2019).
- [14] H. Zhong, Y. Tian, N. Gao, K. Lu, and J. Wu, Ultra-thin composite underwater honeycomb-type acoustic metamaterial with broadband sound insulation and high hydrostatic pressure resistance, *Compos. Struct.* **277**, 114603 (2021).
- [15] S. Qu and P. Sheng, Microwave and acoustic absorption metamaterials, *Phys. Rev. Appl.* **17**, 047001 (2022).
- [16] C. Hopkins, *Sound Insulation* (Butterworth-Heinemann, Oxford, 2007).
- [17] Z. Yang, H. M. Dai, N. H. Chan, G. C. Ma, and P. Sheng, Acoustic metamaterial panels for sound attenuation in the 50–1000 Hz regime, *Appl. Phys. Lett.* **96**, 041906 (2010).
- [18] Y. Xiao, J. Wen, and X. Wen, Sound transmission loss of metamaterial-based thin plates with multiple subwavelength arrays of attached resonators, *J. Sound. Vib.* **331**, 5408 (2012).
- [19] F. Langfeldt and W. Gleine, Optimizing the bandwidth of plate-type acoustic metamaterials, *J. Acoust. Soc. Am.* **148**, 1304 (2020).
- [20] A. S. Ba, A. Kovalenko, C. Aristégui, O. Mondain-Monval, and T. Brunet, Soft porous silicone rubbers with ultra-low sound speeds in acoustic metamaterials, *Sci. Rep.* **7**, 40106 (2017).
- [21] M. N. Andersen, F. Wang, and O. Sigmund, On the competition for ultimately stiff and strong architected materials, *Mater. Des.* **198**, 109356 (2021).
- [22] J. Bauer, A. Schroer, R. Schwaiger, and O. Kraft, Approaching theoretical strength in glassy carbon nanolattices, *Nat. Mater.* **15**, 438 (2016).
- [23] L. Meza, A. J. Zelhofer, N. Clarke, A. J. Mateos, D. Kochmann, and J. R. Greer, Resilient 3D hierarchical architected metamaterials, *Proc. Natl. Acad. Sci. U. S. A.* **112**, 11502 (2015).
- [24] T. Schaedler, A. J. Jacobsen, A. Torrents, A. E. Sorensen, J. Lian, J. R. Greer, L. Valdevit, and W. B. Carter, Ultralight metallic microlattices, *Science* **334**, 962 (2011).
- [25] S. S. Injeti, C. Daraio, and K. Bhattacharya, Metamaterials with engineered failure load and stiffness, *Proc. Natl. Acad. Sci. U. S. A.* **116**, 23960 (2019).
- [26] J. Berger, H. N. G. Wadley, and R. M. McMeeking, Mechanical metamaterials at the theoretical limit of isotropic elastic stiffness, *Nature* **543**, 533 (2017).
- [27] X. Zheng, W. Smith, J. Jackson, B. Moran, H. Cui, D. Chen, J. Ye, N. Fang, N. Rodriguez, and T. Weisgraber, Multiscale metallic metamaterials, *Nat. Mater.* **15**, 1100 (2016).
- [28] G. Ma, C. Fu, G. Wang, P. D. Hougne, J. Christensen, Y. Lai, and P. Sheng, Polarization bandgaps and fluid-like elasticity in fully solid elastic metamaterials, *Nat. Commun.* **7**, 13536 (2016).
- [29] See Supplemental Material at <http://link.aps.org/supplemental/10.1103/PhysRevApplied.20.054015> for details of theoretical derivation, homogenization method, geometric parameters and further discussions for this work, including references [44–48].
- [30] U. G. K. Wegst, H. Bai, E. Saiz, A. P. Tomsia, and R. O. Ritchie, Bioinspired structural materials, *Nat. Mater.* **14**, 23 (2015).
- [31] A. A. Zadpoor, Mechanical performance of additively manufactured meta-biomaterials, *Acta Biomater.* **85**, 41 (2019).
- [32] M. Peng, Z. Wen, L. Xie, J. Cheng, Z. Jia, D. Shi, H. Zeng, B. Zhao, Z. Liang, T. Li, and L. Liang, 3D printing of ultralight biomimetic hierarchical graphene materials with exceptional stiffness and resilience, *Adv. Mater.* **31**, 1902930 (2019).
- [33] M. C. Fernandes, J. Aizenberg, J. Weaver, and K. Bertoldi, Mechanically robust lattices inspired by deep-sea glass sponges, *Nat. Mater.* **20**, 237 (2021).
- [34] L. J. Gibson and M. F. Ashby, *Cellular Solids: Structure and Properties* (Cambridge University Press, Cambridge, 1997).
- [35] J. Wolff, *The Law of Bone Remodeling*, Translated by P. Maquet and R. Furlong (Springer, New York, 1986).
- [36] F. Wang and O. Sigmund, Numerical investigation of stiffness and buckling response of simple and optimized infill structures, *Struct. Multidiscipl. Optim.* **61**, 2629 (2020).
- [37] H. Y. Mak, X. Zhang, Z. Dong, S. Miura, T. Iwata, and P. Sheng, Going beyond the causal limit in acoustic absorption, *Phys. Rev. Appl.* **16**, 044061 (2021).
- [38] M. Pham, C. Liu, I. Todd, and J. Lertthanasarm, Damage-tolerant architected materials inspired by crystal microstructure, *Nature* **565**, 305 (2019).
- [39] N. A. Fleck, Micro-architected materials: Past, present and future, *Proc. R. Soc. London, Ser. A* **466**, 2495 (2010).
- [40] V. S. Deshpande, M. Ashby, and N. Fleck, Foam topology: Bending versus stretching dominated architectures, *Acta Mater.* **49**, 1035 (2001).
- [41] Y. Zhang, X. Qiu, and D. Fang, Mechanical properties of two novel planar lattice structures, *Int. J. Solids Struct.* **45**, 3751 (2008).
- [42] Z. Hashin and S. A. Shtrikman, A variational approach to the theory of the elastic behaviour of multiphase materials, *J. Mech. Phys. Solids* **11**, 127 (1963).
- [43] J. Aizenberg, J. Weaver, M. Thanawala, V. Sundar, D. Morse, and P. Fratzl, Skeleton of *Euplectella* sp.: Structural hierarchy from the nanoscale to the macroscale, *Science* **309**, 275 (2005).
- [44] B. A. Auld, *Acoustic Fields and Waves in Solids* (Krieger Publishing Company, Malabar, 1990).
- [45] P. Langlet, A. C. Hladky-Hennion, and J. N. Decarpigny, Analysis of the propagation of plane acoustic waves in passive periodic materials using the finite element method, *J. Acoust. Soc. Am.* **98**, 2792 (1995).

- [46] A. Bensoussan, J. Lions, and G. Papanicolaou, *Asymptotic Analysis for Periodic Structures* (North-Holland Publishing Co., Amsterdam, 1978).
- [47] F. Fahy and P. Gardonio, *Sound and Structural Vibration* (Academic Press, Oxford, 2007).
- [48] ASTM E2611-09, *Standard Test Method for Measurement of Normal Incidence Sound Transmission of Acoustical Materials Based on the Transfer Matrix Method* (American Society for Testing and Materials, New York, 2009).